Model validation of Phase-Induced Amplitude Apodization Complex Mask Coronagraph for LUVOIR-A in vacuum

Dan Sirbu*[1], David Marx[2], Ruslan Belikov[1], Eduardo Bendek[2], Steve Bryson[1], Brian Kern[2], Kevin Fogarty[1], Olivier Guyon[3], Eugene Pluzhnik[1], Daniel Wilson[2]

[1] NASA Ames Research Center, Moffett Field, Mountain View, CA

[2] Jet Propulsion Laboratory, California Institute of Technology, Pasadena, CA

[3] University of Arizona, Tucson, AZ

ABSTRACT

The Phase-Induced Amplitude Apodization Complex Mask Coronagraph (PIAACMC) is a coronagraph architecture for the next generation of large space telescopes optimized for habitable exoplanet imaging that can achieve attractive theoretical performance with high throughput at small inner working angles (IWA). PIAACMC designs are compatible with large, on-axis, segmented apertures such as the Large UV / Optical/ Infrared A (LUVOIR-A) concept currently being considered by the decadal survey review which would greatly enhance the possibility to achieve statistically significant scientific yields and signal quality for direct imaging exoplanet surveys.

PIAACMC has been recently implemented for LUVOIR-A and is currently being tested in vacuum at JPL's High-Contrast Imaging Testbed (HCIT). In this work, we review the theoretical performance of the PIAACMC instrument designed to meet a 1e-9 raw contrast goal in 10% broadband light in a region from 2-8 L/D both before and after the wavefront control loop. We use empirical measurements from the vacuum testbed to verify the instrument model and its performance including line-of-sight errors, instrument alignment, and fabricated components. In particular, the model verification includes measured sags of the manufactured PIAA mirrors by NuTek. The CMC mask was manufactured at JPL's Microdevices Laboratory and we include surface profile characterization measurement. We assess the impact on performance of the different manufacturing and alignment errors.

Keywords: High-Contrast Imaging, Binary Stars, Wavefront Control, WFIRST, Multi-Star Wavefront Control, Super-Nyquist Wavefront Control

1. INTRODUCTION

Over 4000 known exoplanets have been discovered primarily from the Kepler and TESS misions' transiting surveys and from ground-based radial velocity surveys. The next step for exoplanet science will be the direct imaging of nearby exoplanets to enable characterization of these planets' atmospheres and composition. Direct imaging of exoplanets requires the suppression of both diffracted and scattered light from the host star while passing through as much of the dim planetary companion's light at sufficiently small angular separations and contrast ratios to both detect and characterize the exoplanet through spectroscopy. NASA's next flagship mission will be the Roman Space Telescope which is planned to have a coronagraphic instrument onboard to demonstrate coronagraph technology and high-contrast imaging capability. NASA is currently considering the HabEx[1] and LUVOIR[2] flagship mission concepts for which exoplanet imaging would represent the key science outcome with the goal of reaching performance levels that would enable imaging terrestrial-like planets. LUVOIR-A is an on-axis telescope with a 15-m diameter. Due to its large size, LUVOIR presents technical challenges for the direct imaging of exoplanets. First, LUVOIR will be a segmented telescope which introduces additional diffraction leakage due to the presence of a of its segment gaps and misalignment. Additionally, the LUVOIR-A design is on-axis with a significant obstruction due to its secondary that must be controlled using a coronagraph. LUVOIR-B will be an off-axis telescope with segmentation, and for this case classical PIAA designs have been shown to work very efficiently when evaluated for yields.[3–5] Finally, LUVOIR's large diameter increases its

---

* email: dan.sirbu@nasa.gov

sensitivity to nearby stars – thus coronagraph designs must be robust to tip/tilt sensitivity to efficiently survey nearby stars

PIAACMC[6] has been recently implemented for LUVOIR-A[4, 7, 8] and is currently being tested in vacuum at JPL's High-Contrast Imaging Testbed (HCIT). In this paper, we first review the theoretical performance of the PIAACMC designed for 1e-9 contrast in broadband light in a region from 2-8 λ/D both before and after the wavefront control loop.[4] We then update the model used to design the PIAACMC coronagraph based on empirical measurements taken from the vacuum chamber at HCIT to validate the model with laboratory data. We use empirical measurements from the vacuum testbed to verify the instrument model and its performance including line-of-sight errors, instrument alignment, and fabricated components. In particular, the model verification includes measured sags of the manufactured PIAA mirrors by NuTek and comparison of the design and measured mirror-induced apodizations. The CMC mask was manufactured at JPL's Microdevices Laboratory and we include surface profile characterization measurement. We assess the impact on performance of the different manufacturing and alignment errors. We also compare the measured and expected system Jacobian used for mid-spatial frequency wavefront control. While this paper focuses on comparison of the design model with empirical data, there is also a companion paper at this conference[9] focusing on the latest results obtained in the testbed when operating the wavefront control loop that show unmodulated raw contrast in the dark hole of 1.0e-8 (limited by incoherent ghosting), and a modulated contrast of 5.1e-9 contrast.

This work builds on heritage from previous PIAACMC tests during the preliminary selection phase for the Roman coronagraph instrument,[10] as well as previous PIAA laboratory tests for monolithic apertures tested in vacuum.[11, 12]

2. PIAACMC DESIGN FOR LUVOIR-A

One of the strengths of PIAACMC is that it can enable operation at small inner working angles with lossless apodization.[13] For LUVOIR-A in particular, due to its large aperture a small IWA can open the habitable zone of many stars that are farther; the habitable zones of stars become accessible inversely related to the coronagraph's IWA.[3] For the 2 λ/D IWA of this PIAACMC design compared to 3.5-4 λ/D IWA of baselined LUVOIR-A coronagraphs, up to twice as many habitable zones of target stars would be accessible. The high throughput in addition can also increase scientific yields due to improved photon flux levels allowing better SNR levels or more distant targets. PIAACMC was evaluated as part of the suite of LUVOIR-A coronagraphs and it was shown that its presence can increase yields by 10% by targetting additional stars that are farther and dimmer than with the existing LUVOIR-A coronagraph suite – this opens up a new regime of characterization for LUVOIR. High throughput levels characteristic of PIAACMC are also beneficial for the operation of the wavefront control loop, including faster and more efficient correction of mid-spatial aberrations, as well as improved alignment for the low-order wavefront sensing (LOWFS) loop. Finally, improved throughput benefit post-processing for photon-limited targets. The PIAACMC architecture was developed by Guyon[6] and is summarized in Figure 1. Key components are shown including:

1. remapping PIAA mirrors that generate a mild apodization with an additional, optional conventional post-apodizer, and
2. the complex mask coronagraph (CMC) focal plane mask which is phase-shifting and partially transmissive, and
3. Lyot plane-masksing that blocks regions of constructive interference with destructive interference localized in the open regions of the Lyot mask, and
4. an (optional) inverse PIAA module to recover PSF sharpness at off-axis locations in the science camera plane.

This general PIAACMC coronagraph architecture was adapted as part of a point design to operate with the on-axis LUVOIR-A pupil for the vacuum experiments at JPL's HCIT.[4, 5] This point design is summarized in Figure 2. We describe here the main steps taken to generate the PIAACMC design that was adopted for hardware testing at HCIT and present the sensitivity of this design. For this point design, we are using the inscribed portion of the LUVOIR-A aperture. This decision was driven by simplicity, though in the future fundamental exploration of the coronagraph operator space has shown it should be possible to use the full circumscribed aperture and thus gain up to 20% additional effective aperture area.
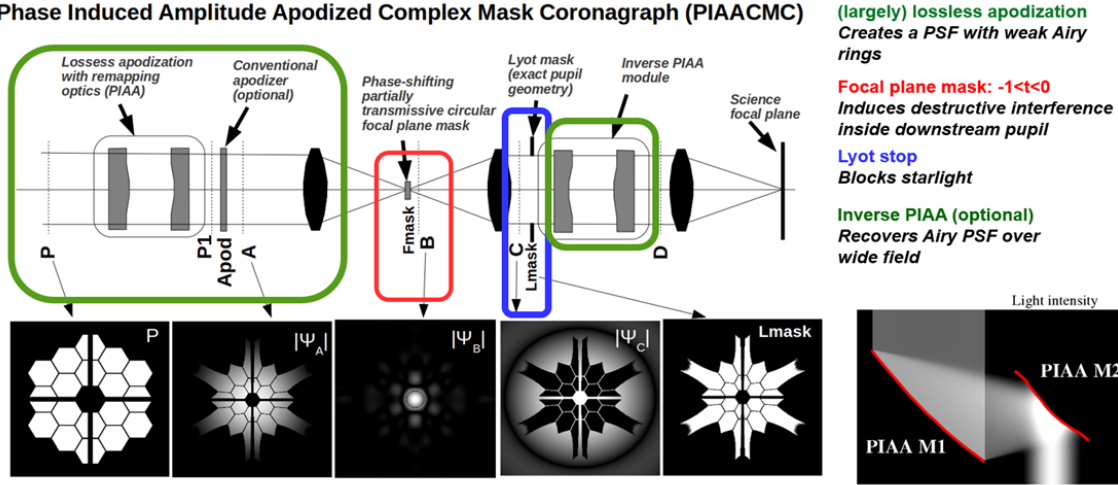
Figure 1: Summary of the PIAACMC coronagraph architecture. Key planes are indicated in the top pane, and corersponding electric fields are shown in the bottom panes.

PIAA apodization: The canonical PIAA is a prolate-spheroidal for monolithic apertures, but for usage with an obstructed pupil such as LUVOIR-A in a PIAACMC architecture mode we are using an iterative numerical search to identify a monotonic apodization that is compatible with an ideal CMC mask. In addition, we are using a circularly symmetric apodization profile which has a number of benefits including ease of manufacturing for the PIAA mirrors including on-axis PIAA mirrors and ease of alignment with the rest of the system (though at the requirement of offloading control of diffraction from struts and segments to the combined wavefront control system and Lyot stop). This mild apodization resulted in relatively small sags on the PIAA mirrors reaching up to 70 um specification near the edges. Alternate apodizations that were considered were a donut-shaped which had an extremum in-between the inner and outer portions of the pupil and arose for smaller inner-working angles. The final, monotonic apodization was chosen with an inner working angle of 1.9 λ/D (in system-units) to increase the expected jitter robustness of the PIAACMC architecture.

CMC mask: The focal plane mask was designed using nonlinear numerical optimization techniques using the csim package.[4] The initial exploration space of the design used the ideal, π-phase shifting CMC at the focal plane mask to identify the best theoretical robustness to tip/tilt. This was then replaced by a mask that was numerically optimized to approximate this ideal CMC. The final CMC consists of a set of hexagonal segments. Each of these hexagonal segments has an optimized sag, and is designed being fed as input the PIAA apodization and central obstruction. Therefore, the CMC also does not account for the struts and segments of the LUVOIR-A aperture. In addition, hybrid approaches using the CMC design approach are possible as well as optimizing for additional metrics such as tip/tilt and low-order aberration robustness, and jointly optimizing the apodization and CMC (which were treated independently here).

Lyot mask: The Lyot mask is designed by ray-tracing the LUVOIR-A pupil through the PIAA apodization then enlarging the features of the remapped pupil. We have considered both a version that includes re-mapped segments and struts, and found that re-mapping the segments did not substantially improve performance to account for the loss of throughput from the enlargement of the segments. As a result, the Lyot stop design chosen used only enlarged, remapped struts (but not segments). The Lyot stop was placed to be conjugate to the re-mapped pupil at PIAA-2.

DM solution: the shape of the DM is an integral part of the design; the DM compensates for residual diffraction leakage from the struts, segments, and any Fresnel propagation effects between the PIAA mirrors as well as other intermediate optics. Only 1-DM is used in this design placed at a plane conjugate to the exit PIAA-2 mirror (different conjugate locations were considered; for a single DM, conjugation to PIAA-2 was slightly preferred to PIAA-1 (in terms of DM stroke usage), and with improved computational profile compared

to intermediate locations. For a 2-DM system, the optimal locations identified would have been DMs conjugate to each of PIAA-1 and PIAA-2).
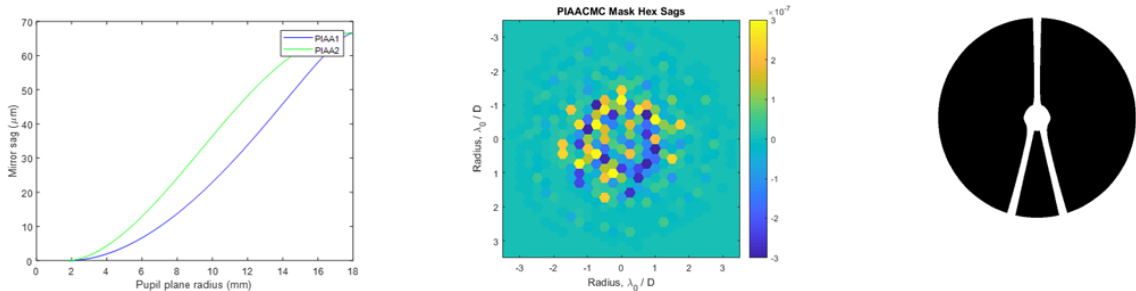

Figure 2: Summary of the PIAACMC point design for the LUVOIR-A aperture. *Left*: PIAA mirror sags that generate a monolithic apodization. *Center*: CMC mask with optimized hexagonal segment sags. *Right*: Re-mapped, enlarged Lyot stop through PIAA apodization.
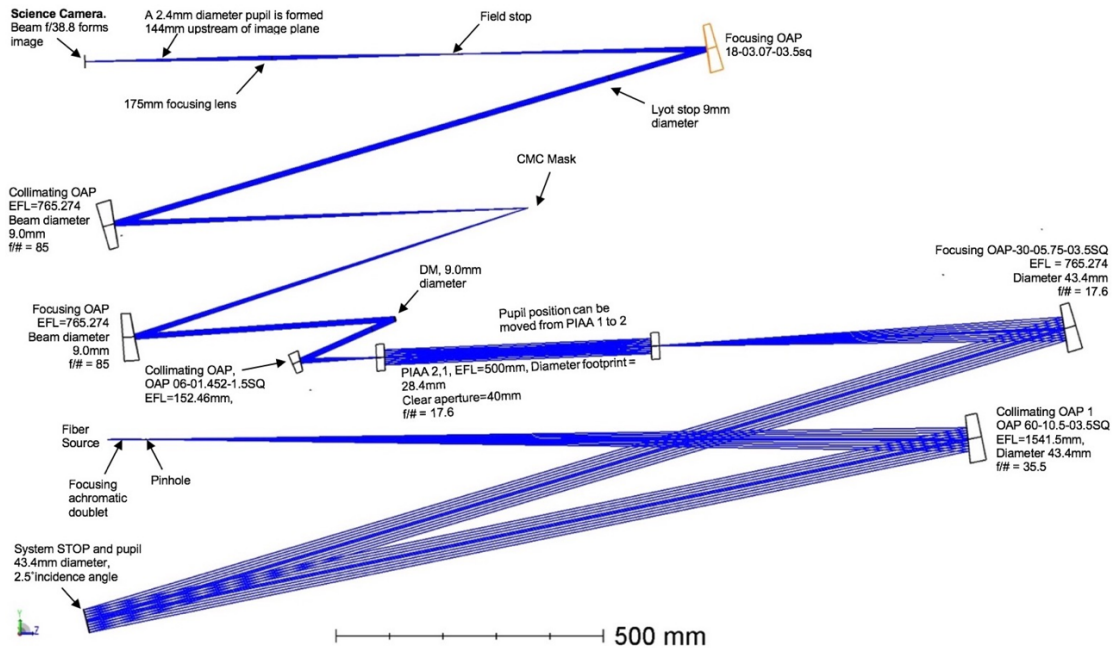

Figure 3: Full, folded layout of the LUVOIR-A PIAACMC coronagraph as implemented at JPL's HCIT.
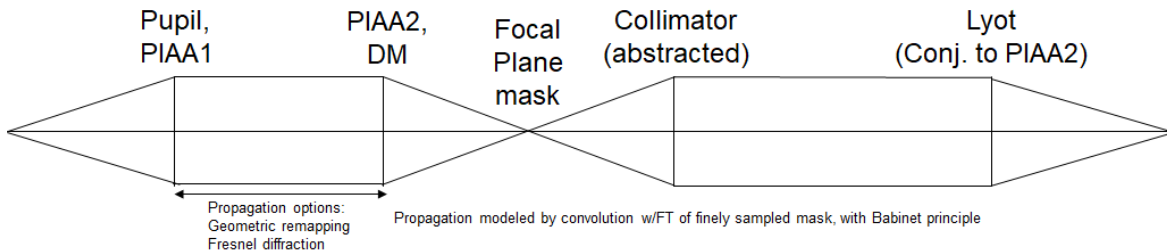

Figure 4: Compact layout used to model the PIAACMC coronagraph. Propagation options between the PIAA mirrors include simple raytracing and full diffraction propagation, or using empirical phase retrieval measured using a Gerchberg-Saxton process from the testbed.

3. PIAACMC HARDWARE & MODEL

The PIAACMC coronagraph design was implemented in the vacuum chamber at HCIT using a folded layout as shown above in Figure 3. More details about the PIAACMC hardware implementation are available in previous papers as well as the companion paper in this conference. We focus here on describing the fabricated hardware focusing on the interface between component characterization and the testbed model, with the goal of showing estimated design performance with an updated model (compared to the design) that takes as input empirical measurements.

Briefly, the PIAACMC coronagraph follows a Lyot architecture. The fiber source is collimated by OAP-1 onto the LUVOIR-A pupil scaled to 43.6 mm diameter and manufactured with a carbon nanotube process to enable the small feature sizes of 20 um required for the pupil segmentation gaps. OAP-2 focuses and re-magnifies the beam for entrance to the key coronagraph component, which is the PIAA-tube assembly. The PIAA-tube consists of two confocal, on-axis parabolic mirrors that generate the telescope apodization and contains the two PIAA mirrors. The PIAA tube takes advantage of the existence of the on-axis obstruction and features an input beam focused at the vertex of PIAA-1 passing through the PIAA-2 obstruction. PIAA-1 is a collimating mirror conjugate to the LUVOIR surrogate pupil with the PIAA sag profile superimposed on-top of a parabola with effective focal length of 0.5-m matching the collimated beam propagation distance between the PIAA optics. Likewise, the beam is focused by the PIAA-2 mirror at the exit focus passing through an opening corresponding to the obstruction at PIAA-1. The beam footprint at both PIAA-1 and PIAA-2 is 14.2 mm. OAP-3 re-magnifies the beam onto the 952-actuator Boston MEMS circular DM, which is located conjugate to PIAA-2. DM registration has shown that the beam spans approximately 26 actuators the DM. OAP-4 generates a slow beam with f/85 incident onto the reflective CMC mask, and re-collimated by OAP-5. The Lyot mask is in collimated space conjugate to PIAA-2, and a final field stop assembly is available to reduce the dynamic range required for imaging onto the Andor NEO science camera. The plate scale measured on the science camera is 6.2 pixels per λ/D (system units).

The coronagraph is modelled using a compact layout that efficiently approximates the full layout on HCIT. Propagation options between PIAA mirrors include (1) simple remapping via raytracing, or (2) full Fresnel-propagation using the PIAA mirror sags. Alternatively, the electric field at the PIAA-2 exit can be an empirical measurement using the Gerchberg-Saxton phase-retrieval output available from the testbed[14] at the DM conjugate. The DM is collocated with the PIAA-2 exit electric field in this layout, and between the DM and camera we have a pure Lyot architecture but using the reflective CMC mask. For propagation through the focal plane, we perform convolution with a finely-sampled CMC mask applying Babinet's Principle (with the effect of the mask at the pupil plane precomputed for all wavelengths for efficient propagation). Full testbed compatibility is verified by including out-of-plane Fresnel propagation effect for the worst optic and checking correctability in closed-loop wavefront control mode. The model is sampled at the pupil plane to match the testbed camera pixels across the pupil.

The PIAACMC hardware is shown in Figure 5. This includes the PIAA-tube assembly fabricated by NuTek optics. Inteferometric measurements of the wavefront figure error shows an RMS wavefront error of $\lambda/10$ (65 nm) RMS compared to the original specification of $\lambda/30$ (20 nm) RMS. However, the residual error is dominated by spherical aberration modes that are almost completely circularly symmetric. Feeding this error into the system model and running wavefront control with the measured system error showed that this error is well-corrected within the DM stroke requirements to within the milestone contrast requirements of 1e-9 raw contrast in the D-shaped region of 2-8 λ/D. Additionally, residual alignment errors after DM flattening are fed into the model through the empirical input in the form of the testbed phase-retrieval estimate. The wavefront control loop is operated with Electric Field Conjugation (EFC), using empirical DM registration data available from the testbed. To determine the electric field estimate to compute the DM solution, pairwise probing is used with narrowband filters. The reflective CMC mask was fabricated at JPL's Microdevices Laboratory via e-beam lithography[15] on a PMGI substrate with a 200 nm resolution (matching the design specification); the CMC mask features 24 hexagons from top to bottom with a 1.4x1.4 mm field of view opening in which the beam is etched to a bias level. A grid of such squares is laid out 7x7 with the CMC pattern at the center to enlarge the field of view of the CMC at which the bias level has been etched. Finally shown are the carbon nanotube LUVOIR-A pupil surrogate and the Lyot stop. The surrogate pupil is 43.6 mm in diameter and manufactured with a carbon nanotube growth

process to enable specification of its small 20 um segment gap features and is reflective. The Lyot stop which is the remapped version of the LUVOIR struts and obstruction and a undersized circular stop of 0.9 fractional size was manufactured with the same process with a 9 mm diameter.
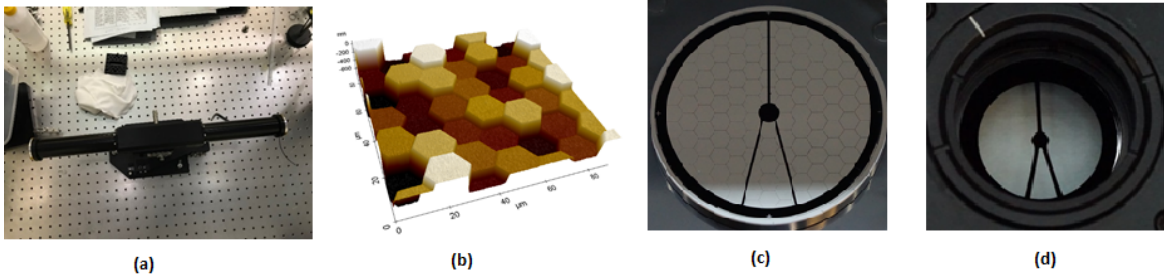

Figure 5: Summary of the hardware fabricated for the PIAACMC coronagraph testbed at HCIT. *(a)*: On-axis, confocal PIAA-tube assembly manufactured by NuTek. *(b)*: reflective CMC mask manufactured on PMGI via e-beam lithography at JPL's Microdevices lab. *(c)*: reflective LUVOIR-A pupil with 43.6 mm diameter surrogate manufactured by Lambda Consulting with a carbon nanotube growth process and featuring 20 um segment gaps. *(d)*: Lyot stop with 9 mm beam diameter footprint manufactured with the same process as the pupil surrogate.
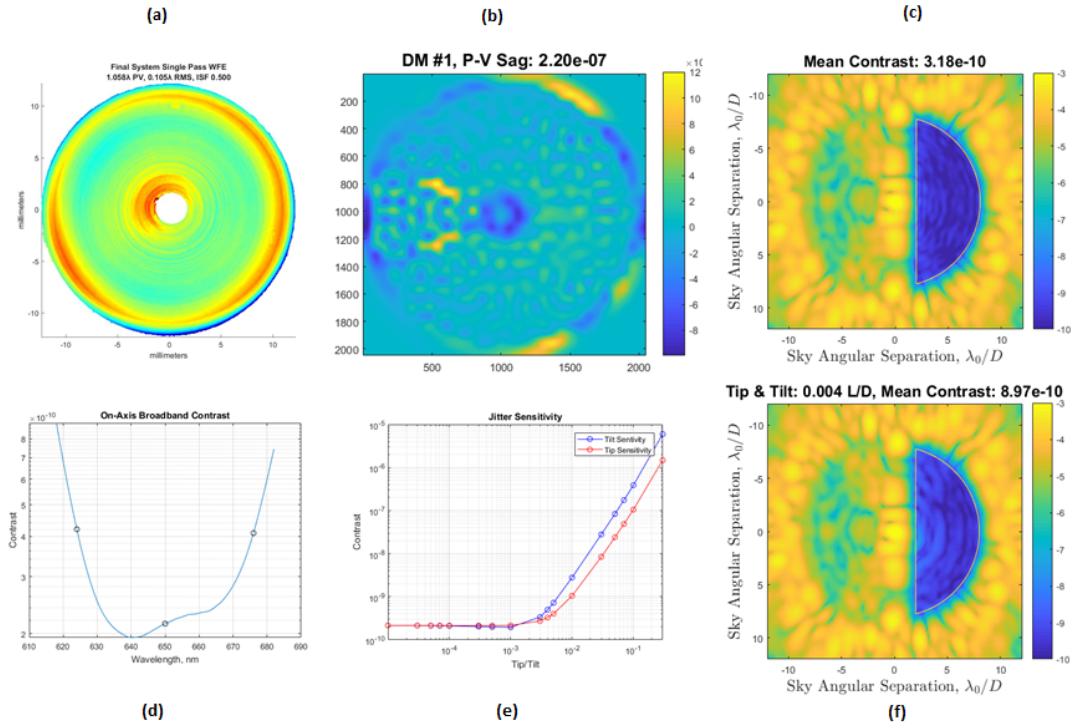

Figure 6: Wavefront control solution for the model updated through empirical inputs. *(a)*: System wavefront error measured through the PIAA optics. *(b)*: DM solution showing correctability of the PIAA optics with mild stroke requirements of 220 nm P-V and 34 nm RMS. *(c)*: corresponding dark hole meeting milestone contrast requirement of 1e-9 in 10% bandwidth. *(d)*: chromaticity of contrast across the dark hole with indicated optimized wavelengths in 3.3% filter bands. *(e)*: tip/tilt sensitivity of the DM solution showing that the milestone contrast level can be maintained at an expected level of 0.004 λ/D per axis or better. *(f)*: corresponding dark hole with degradation due to a jitter level of 0.004 λ/D.

4. PIAACMC MODEL VALIDATION

We validate the model and design by comparison of output with testbed measurements. The model apodization generally matches the design apodization after accounting for a 20% measured undersizing of the measured apodization – this significant undersizing at PIAA-2 can be explained by a slight beam undersizing of the input beam at PIAA-1. Model-based raytracing of the segments and struts through PIAA matches empirical measurements to better than 0.28%. We then compare the on-axis and off-axis model and empirical PSFs and suppression in both the Lyot planes and the core leakage due to the CMC mask. We show correctability of different types of errors consistent with characterization of the manufactured CMC and with alignment precision as expected in the testbed. Finally, we use empirical data of testbed stability both in terms of fast jitter and long-term drifts to approximate the achievable contrast limits in the testbed.

PIAA apodization: after alignment of the PIAA-tube onto the testbed, the first task was to validate the design apodization. This was achieved by setting the camera to image the conjugate exit PIAA-2 plane, and comparing intensity measurements with the model. First, the accuracy of the raytracing through the PIAA optics was compared by superimposing the remapped LUVOIR-A pupil onto the empirical intensity obtained from the pupil-imaging camera as shown in Figure 7. Matching the remapped pupil's segments shows a precision of 1 pixel across the 350 pixel pupil which corresponds to a remapping accuracy of segmentation features near the central obstruction of better than 0.28%.

The PIAA apodization is also compared by azimuthally averaging the empirical intensity delivered at the re-imaged, exit PIAA-2 plane with the model. Two different model apodizations are used here: (1) the ideal, design PIAA apodization from which PIAA sags were computed for manufacturing specification, and (2) intensity from the model output after feeding in measured PIAA sag profiles and performing Fresnel propagation between the PIAA mirrors. These azimuthal averaged curves are shown below in the left pane of Figure 8. The comparison demonstrates good agreement of the apodization with the significant exception of an undersizing of the apodization by approximately 20% at the outer edges. This undersizing can be accounted for due to the remapping effect of the PIAA mirrors for a slightly undersized input beam, resulting in an even larger undersizing at the PIAA exit mirror. To see this effect, a scan of the input beam for different undersizing factors up to 3% is shown in the right pane of Figure 8. The apodization is undersized by 20% at the PIAA exit when the input beam is undersized by 2%.
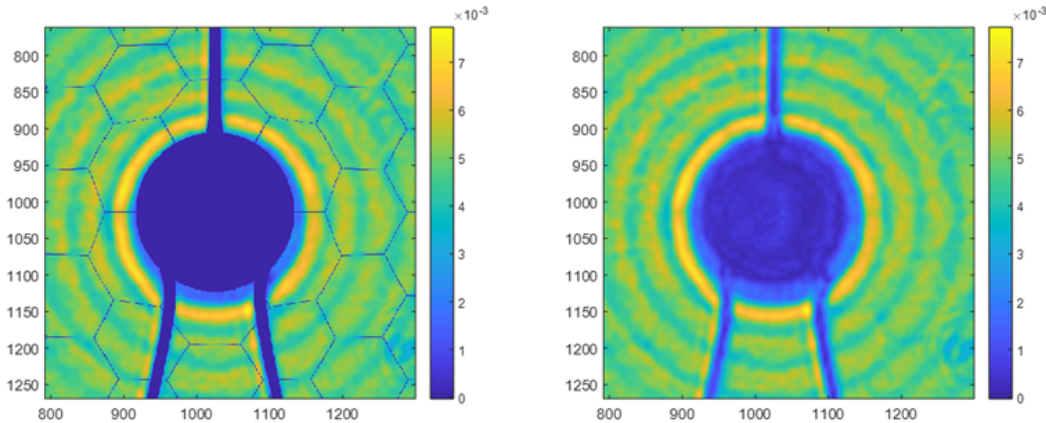

Figure 7: Validation of PIAA apodization by comparison of remapped features to empirical data: *Left* with super-imposed model remapping of pupil & segments, *Right* raw pupil-imaging intensity measurement from the camera.

DM & PSF response: another validation of the testbed can be obtained by comparing the empirical PSF with the model PSF for the PIAA apodization for both an on-axis PSF and at off-axis locations as the source moves laterally. These PSFs are obtained with the aligned PIAA-tube and without a CMC mask (using a flat
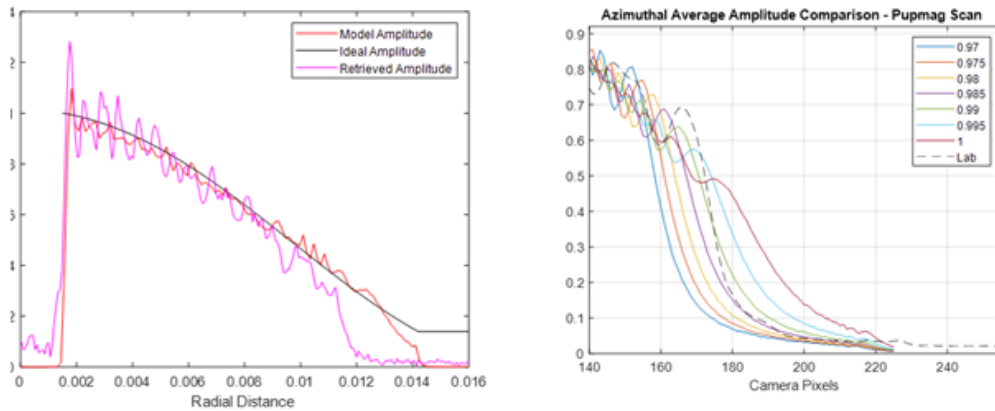
Figure 8: Validation of PIAA apodization by comparison of the azimuthally averaged intensity across the PIAA-2 exit plane: *Left*, azimuthally averaged apodizations for the ideal design (raytracing), full model propagation through PIAA sags (Fresnel), and finally the azimuthally averaged apodization; *Right*, raw pupil-imaging intensity measurement from the camera, and *Right* demonstration of the effect of undersizing of the beam at the PIAA input by scanning different input beam undersizing factors up to 3% and plotting the output apodization showing undersizing of up to 20% at the PIAA exit.

reflective surface at the focal plane location). In Figure 9, we see good agreement in both the location of the off-axis PSFs as well as the off-axis distortion induced by the mild PIAA apodization.

After accounting for the PIAA PSF, the DM response is validated next. This is achieved by placing a probe pair on the DM and comparing the model response with the testbed resopnse. Next, a constant amplitude sine wave is placed across the DM sweeping through increasing sinusoidal frequencies to obtain a match of the influence function from comparing the probe amplitude's fall-off envelope. Both of these tests are shown in Figure 10.

CMC suppression: the next key element of the model to be validated is the CMC mask and in particular the suppression delivered by the CMC. This suppression factor can be measured at either the Lyot plane by computing the remaining energy in the open regions of the Lyot stop (which should see destructive interference) as well as by comparison of the suppression factor of the core after passing through the CMC mask. A CMC prototype was initially manufactured that showed a factor of 3x energy across the Lyot plane compared to the expected model built from interferometric Wyko measurement data of the mask. For a more quantitative performance, azimuthally averaged curves of the measured intensity across the Lyot plane are shown with normalization with respect to the no-CMC measurement (which is also fed as the input, empirical apodization into the model). An updated version of the mask showed improvement and agreement at both the Lyot plane and at the focal plane as seen in Figure 11.

Testbed stability: a key uncertainty factor in the coronagraph design was the expected natural stability level in the testbed as no LOWFS would be available to stabilize the system beyond this naturally occurring testbed stability (which was estimated at 0.004 λ/D). To validate performance at the measured testbed stability levels, both the long-term drift and the fast jitter levels were measured for the unocculted testbed PSF. Fast centroid measurements of the PSF core represent the jitter levels, which were measured as 0.008 λ/D across the x-axis (along the table direction) and 0.006 λ/D across the y-axis (perpendicular to the table direction). These testbed measurements are shown in Figure 12. The long-term drift measurement shows that after a period of approximately 20 hours after a disturbance, the testbed reaches a long-term stable level. The jitter levels are slightly higher than expected a priori – once the measured testbed jitter levels are introduced into the model simulation sensitivity curves shown earlier in Figure 6, the expected contrast level in the dark hole is 3e-9.

CMC errors: another key source of errors can arise out of misalignment of the CMC mask as well as different types of fabrication errors (e.g., random sag errors, bias errors, etc.) as well as knowledge errors between the
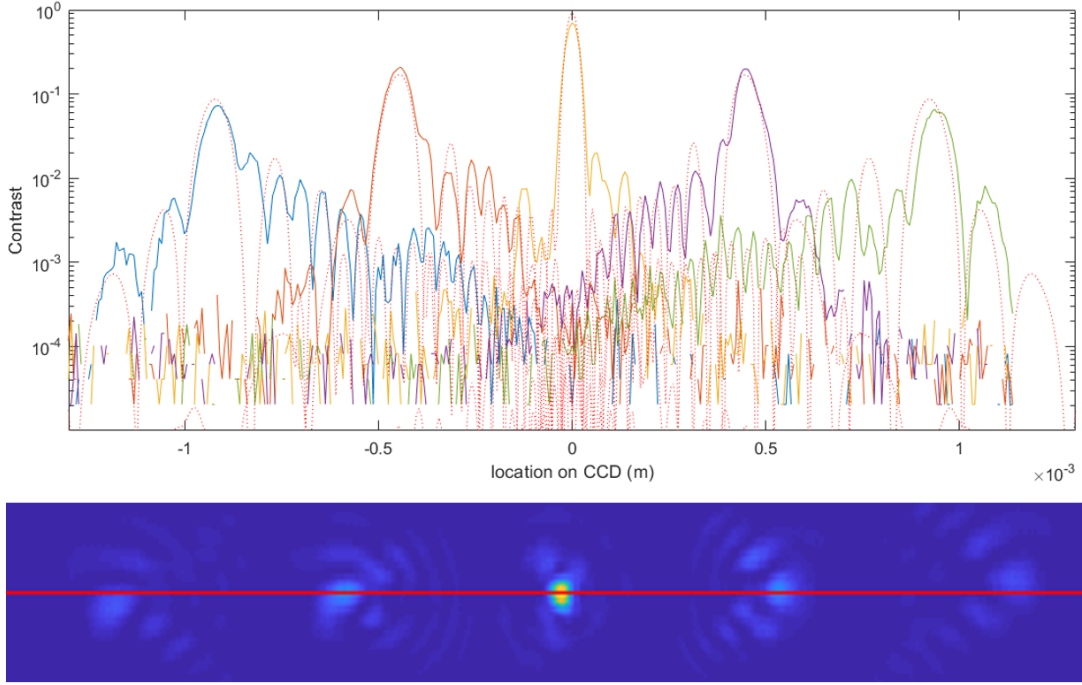
Figure 9: Comparison of the PSF response between model and testbed by scanning the source position laterally : *Bottom* mosaic of the empirical PSFs at different lateral source scan positions, and *Top* cross-section comparison between the empirical PSFs and the corresponding model PSF response.
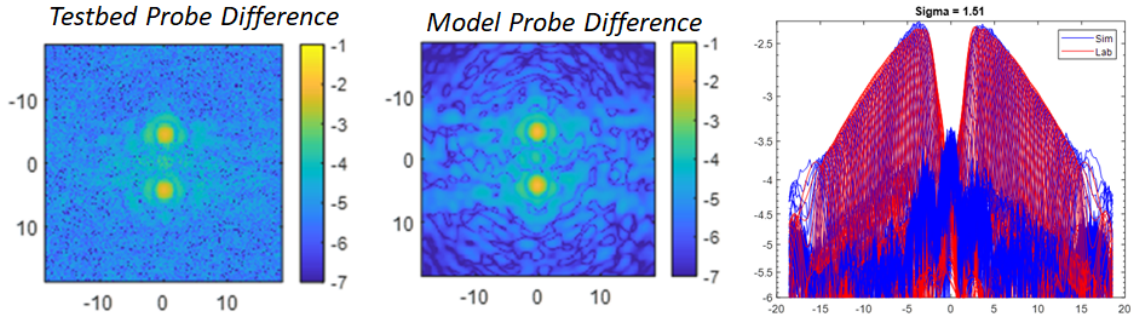

Figure 10: Comparison of the empirical and model DM responses: *(Left)* empirical probe pair difference, *(Center)* model probe pair difference, *(Right)* cross-section comparison through empirical and probe pair differences at best-match influence function Gaussian width (sigma).

model and the testbed related to these types of errors. We have measured the alignment errors expected from the CMC alignment routine which equalizes and minimizes the energy at the Lyot plane and have found that approximately a 0.5 λ/D alignment error can be expected in the lateral directions. We have introduced lCMC misalignment up to this level into the model, and the wavefront control loop is able to correct for these errors even when the misalignment errors are not known explicitly. Defocus errors are correctable to 1e-9 contrast levels with up to 0.1 waves of defocus input to the system. In addition, other alignment errors such as flips, rotations, and measured CMC characterization errors (deviations from the design) have been fed into the model and have found these are correctable by EFC in closed-loop and to 1e-9 raw contrast without explicit knowledge of the specific error.

Probe validation: one additional model validation test we report on is comparing an empirical Jacobian
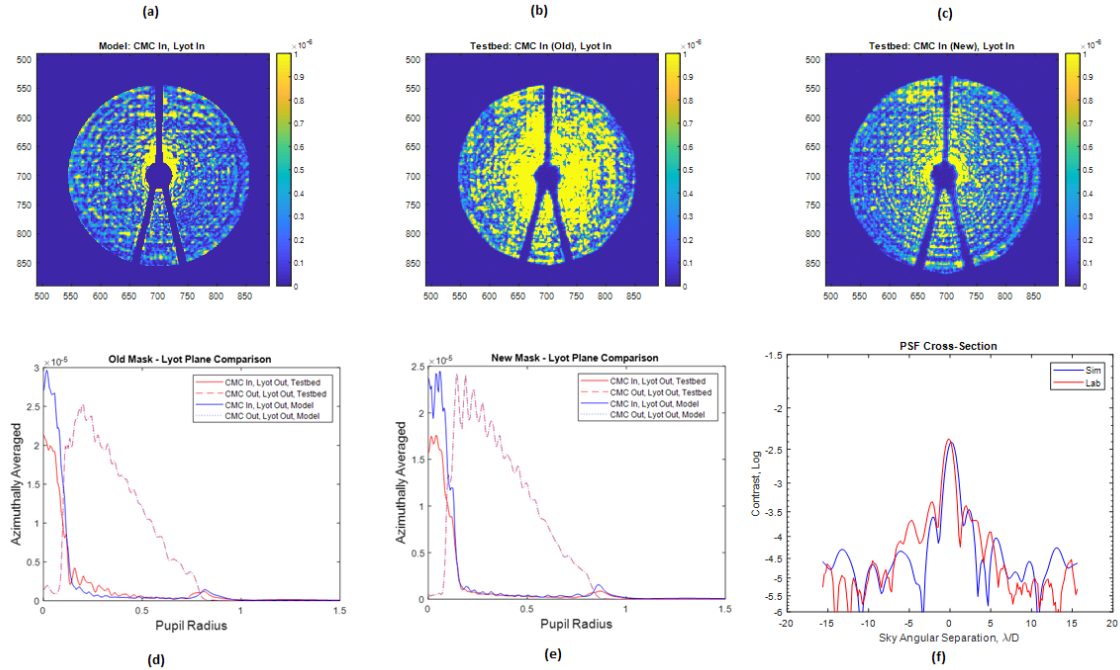
Figure 11: CMC suppression by comparison of design and empirical measurements. *(a)*: measured intensity at the Lyot plane for the first CMC prototype showing additional leakage *(b)*: model intensity at the Lyot plane for the characterized CMC mask showing a smaller amount of leakage than measured from the first CMC prototype *(c)*: measured intensity from the second CMC mask showing improvement in suppression of energy at the Lyot mask by a factor of 3x, emph(d): azimuthal cross-section comparison between the original CMC prototype and the expected leakage from the model showing additional empirical leakage. *(e)*: azimuthal cross-section comparison between the final CMC mask showing agreement in suppression across the Lyot plane·(f): comparison of the empirical and model PSF cores after propagation through the updated CMC mask.
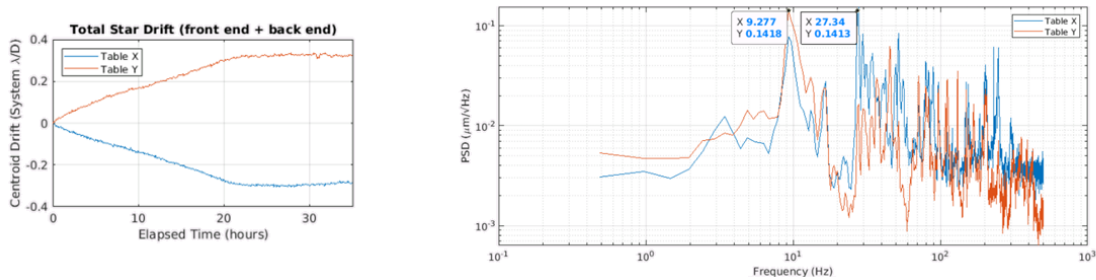

Figure 12: Measured testbed stability in terms of both: *(Left))* Long-term drift, and *(Right)* Fast jitter levels across each optical table axis.

survey by poking each of the actuators illuminated by the input beam by up to 1V with the pure model Jacobian. The empirical response is obtained by performing standard probe-pair based electric field estimation for each of the actuator pokes while randomizing the poke pattern and subtracting the estimate corresponding a reference (flat) DM setting to obtain the change in electric field (ΔE). The set of reference DM settings can also be used to determine the stability of the EFC estimate for the same DM pattern over time. Figure 13 shows the comparison of a single change in electric field due to the same actuator poke applied to the testbed and the model. A complex correlation coefficient for each actuator poke can be computed by comparison of the change in electric field in the two cases. For most actuators, there is good agreement between the two as can be seen in the poke test in Figure 13 – though for a a few of the weaker actuators, the correlation between the electric

fields is worse.

5. CONCLUSIONS

We have reviewed the design and theoretical design performance of the PIAACMC coronagraph that has been recently implemented for LUVOIR-A and is currently being tested in vacuum at JPL's High-Contrast Imaging Testbed (HCIT). A model of the coronagraph has been built that uses empirical measurements from the testbed to best reflect the expected empirical performance for the as-built PIAACMC coronagraph. In addition, we have performed model validation by comparing the empirical and model results for key individual elements of the coronagraph including the PIAA apodization, the DM and the PSF response, the CMC suppression at both the Lyot and PSF planes, the testbed stability, and probe estimate comparisons of individual poke estimates for validation of the system's Jacobian response. The companion paper[9] shows current experimental results wit

ACKNOWLEDGMENTS

REFERENCES

[1] B. S. Gaudi, S. Seager, B. Mennesson, A. Kiessling, K. Warfield, G. Kuan, K. Cahoy, J. T. Clarke, S. Domagal-Goldman, L. Feinberg, O. Guyon, J. Kasdin, D. Mawet, T. Robinson, L. Rogers, P. Scowen, R. Somerville, K. Stapelfeldt, C. Stark, D. Stern, M. Turnbull, S. Martin, O. Alvarez-Salazar, R. Amini,
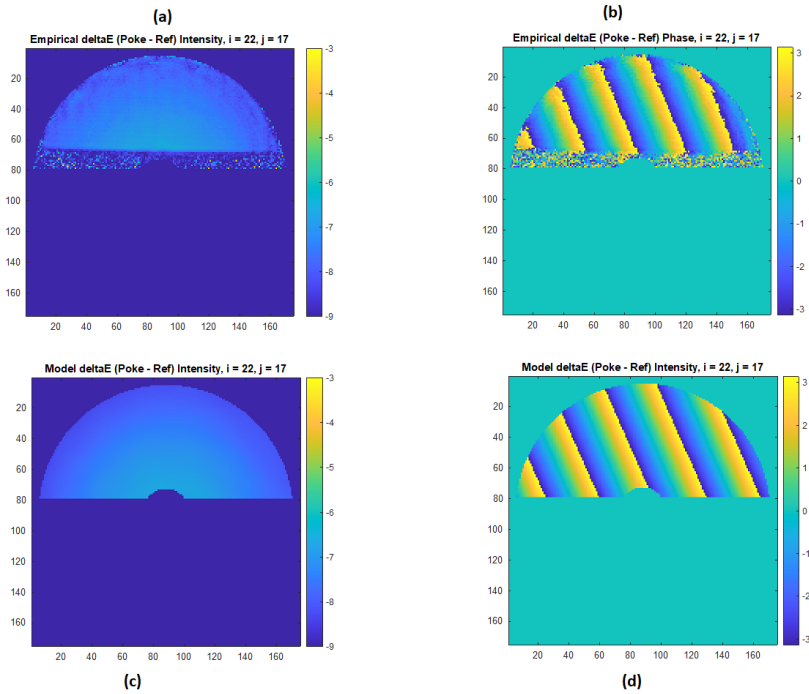
Figure 13: Comparison of change in electric field induced by an actuator poke compared to the reference (flat) DM setting: *(a))* change in empirical intensity, *((b))* change in empirical phase for the induced electric field, *(c))* change in model intensity, *((d))* change in model phase for the induced electic field.

W. Arnold, B. Balasubramanian, M. Baysinger, L. Blais, T. Brooks, R. Calvet, V. Cormarkovic, C. Cox, R. Danner, J. Davis, L. Dorsett, M. Effinger, R. Eng, J. Garcia, J. Gaskin, J. Harris, S. Howe, B. Knight, J. Krist, D. Levine, M. Li, D. Lisman, M. Mandic, L. Marchen, C. Marrese-Reading, J. McGowen, A. Miyaguchi, R. Morgan, B. Nemati, S. Nikzad, J. Nissen, M. Novicki, T. Perrine, D. Redding, M. Richards, M. Rud, D. Scharf, G. Serabyn, S. Shaklan, S. Smith, M. Stahl, P. Stahl, H. Tang, D. Van Buren, J. Villalvazo, S. Warwick, D. Webb, R. Wofford, J. Woo, M. Wood, J. Ziemer, E. Douglas, V. Faramaz, S. Hildebrand t, T. Meshkat, P. Plavchan, G. Ruane, and N. Turner, "Habitable Exoplanet Observatory Final Report," tech. rep., Jet Propulsion Laboratory, August 2019.

[2] D. Fischer, B. Peterson, J. Bean, D. Calzetti, R. Dawson, C. Dressing, L. Feinberg, K. France, O. Guyon, W. Harris, M. Marley, V. Meadows, L. Moustakas, J. O'meara, I. Pascucci, M. Postman, L. Pueyo, D. Redding, J. Rigby, A. Roberge, D. Schiminovich, B. Schmidt, K. Stapelfeldt, C. Stark, and J. Tumlinson, "LUVOIR Final Report," tech. rep., NASA, 2019.

[3] C. Stark *et al.*, "The exoearth yield landscape for future direct imaging space telescopes," *JATIS* **2**(5), 2019.

[4] R. Belikov, D. Sirbu, C. Henze, C. STark, R. Vanderbei, and E. Bendek, "Piaa coronagraph designs for segmented apertures, robust to low-order aberrations," *Proc. SPIE* **11117**, 2019.

[5] D. Sirbu, R. Belikov, C. Henze, G. ruane, K. Fogarty, and O. Guyon, "Performance and sensitivity of piaa coronagraphs for future segmented space telescopes," *SPIE* **114433X**, 2020.

[6] O. Guyon, P. Hinz, E. Cady, R. Belikov, and F. Martinache, "High performance lyot and piaa coronagraphy for arbitrarily shaped apertures," *ApJ* **780**(171), 2013.

[7] R. Belikov, E. Bendek, D. Sirbu, E. Pluzhik, S. Bryson, B. Kern, D. Marx, D. Wilson, O. Guyon, and J. Knight, "Laboratory demonstration of high contrast using piaacmc on a segmented aperture," *NASA Exoplanet Program White Paper* **https://exoplanets.nasa.gov/internal$_r$esources/808$_P$$IAACMC_T$$DEM2016_W$$P_v6_s$$igned.pdf**, 2016.

[8] R. Belikov, S. Bryson, D. Sirbu, O. Guyon, E. Bendek, and B. Kern, "Design and performance analysis of a piaacmc coronagraph on a segmented aperture," *Proc. SPIE* **106981H**, 2018.

[9] D. Marx, R. Belikov, D. Sirbu, B. Kern, C. Prada, and D. Wilson, "Results from the laboratory demonstration of a piaacmc coronagraph with a segmented aperture," *Proc. SPIE* **11823**, 2021.

[10] B. Kern, D. Wilson, O. Guyon, R. Muller, K. Balasubramanian, E. Sidick, I. Poberezhskiy, and R. Belikov, "Phase-induced amplitude apodization complex mask coronagraph mask fabrication, characterization, and modeling for wfirst-afta," *JATIS* **2**(1), 2016.

[11] B. Kern, D. Wilson, O. Guyon, R. Muller, K. Balasubramanian, E. Sidick, I. Poberezhskiy, and R. Belikov, "Laboratory demonstration of phase induced amplitude apodization (piaa) coronagraph with better than 1e-9 contrast," *Proc. SPIE* **8864**, 2013.

[12] D. Sirbu, S. Thomas, R. Belikov, *et al.*, "Excede technology development iv: Demonstration of polychromatic contrast in vacuum at 1.2 l/d," *Proc. SPIE* **9605**, 2015.

[13] O. Guyon, "Phase-induced amplitude apodization of telescope pupils for extrasolar terrestrial planet imaging," *Astronomy and Astrophysics* **404**, 2003.

[14] D. Marx, E. Cady, A. J. E. Riggs, C. Prada, B. Kern, B.-J. Seo, and F. Shi, "Shaped pupil coronagraph: disk science mask experimental verification and testing," *Proc. SPIE* **1069849**, 2018.

[15] D. Wilson, R. Muller, P. Echternach, and J. Backlund, "Electron-beam lithography for micro- and nano-optical applications," *Proc. SPIE* (68), 2005.